Quantitative Study on Current-Induced Effect in an Antiferromagnet Insulator/Pt Bilayer Film

Pengxiang Zhang, Joseph Finley, Taqiyyah Safi, and Luqiao Liu[*]

Department of Electrical Engineering and Computer Science, Massachusetts Institute of Technology, Cambridge, Massachusetts 02139, USA

A quantitative investigation of the current-induced torque in antiferromagnets represents a great challenge due to the lack of an independent method for controlling Néel vectors. By utilizing an antiferromagnetic insulator with the Dzyaloshinskii-Moriya interaction α-Fe$_2$O$_3$, we show that the Néel vector can be controlled with a moderate external field, which is further utilized to calibrate the current-induced magnetic dynamics. We find that the current-induced magnetoresistance change in antiferromagnets can be complicated by resistive switching that does not have a magnetic origin. By excluding nonmagnetic switching and comparing the current-induced dynamics with the field-induced one, we determine the nature and magnitude of current-induced effects in Pt/α-Fe$_2$O$_3$ bilayer films.

Electrical control and detection of magnetic ordering inside antiferromagnets has attracted considerable interest for potential advantages in operating speed and device densities. Current-induced magnetic switching has recently been reported in both metallic [1–7] and insulating [8–11] antiferromagnetic systems. In the former case, special crystal symmetries are utilized for realizing staggered spin-orbit torque, while in the latter one, the spin torque from an adjacent heavy metal layer is utilized for inducing magnetic dynamics. In these studies, anisotropic magneto-resistance, spin Hall magnetoresistance (SMR), or the related planar Hall resistance is generally employed to characterize the electrically induced 90° Néel vector switching. However, unlike ferromagnetic systems, where the current-induced spin torque is calibrated by using an external magnetic field as a standard [12–14], a quantitative relationship between the change of resistance value and the magnitude of spin torque in antiferromagnets remains to be built. So far x-ray based imaging techniques, which require specialized facilities, have to be utilized to determine the ratio of switched magnetic domains [2,7,8,10]. Therefore, there is an urgent need for the development of an electrical measurement method that can be used to quantify the magnitude of current-induced effects in antiferromagnets.

α-Fe$_2$O$_3$ is a well-studied antiferromagnetic insulator [15–17], with a high Néel temperature (955 K) and strong antiferromagnetic exchange interaction (effective exchange field 900–1000 T). As shown in Fig. 1(a), α-Fe$_2$O$_3$ has a trigonal crystal structure, and the two spin sublattices are stacked alternatively along the (0001) direction. It is well known [18] that, at room temperature, α-Fe$_2$O$_3$ exhibits an easy-plane anisotropy which has a very weak ferromagnet-ism ($M_s \sim 2$ emu/cm^3) due to the Dzyaloshinskii-Moriya

interaction, which causes a $<0.1°$ in-plane canting angle between magnetic moments of the two sublattices. Because of the very weak magnetic anisotropy within the basal plane [18], the spin-flop field for aligning the Néel vector perpendicular to the external field direction in α-Fe$_2$O$_3$ can be very low (<1 T), providing a convenient way for controlling the magnetic ordering orientation. In the meantime, the small net moment (M) is perpendicularly oriented with respect to the Néel vector (N) direction, allowing us to separate the different contributions from M and N to magnetic dynamics and transport effects such as SMR. Therefore, α-Fe$_2$O$_3$ represents a nice antiferromagnetic material platform, enabling us to characterize the electrically induced magnetic dynamics by comparing it to field-induced ones.

We grew α-Fe$_2$O$_3$ films on α-Al$_2$O$_3$ (0001) substrates with magnetron sputtering and postdeposition annealing. As shown in Fig. 1(b), despite the lattice mismatch of ~5.8%, epitaxial α-Fe$_2$O$_3$ (0001) films were obtained. The magnetization hysteresis curves measured with a superconducting quantum interference device (SQUID) magnetometer at 300 K are illustrated in Fig. 1(c), which show a small M_s of around 1.5–2 emu/cm^3 and a coercive field of 500–1000 Oe within the entire thickness range of 10–120 nm, which is consistent with previously reported values [18,19]. In order to study current-induced switching and observe SMR, we sputter 5 nm Pt on α-Fe$_2$O$_3$ films and fabricate Hall bars of various widths [Fig. 1(d)], with the voltage and current channels aligned along the [10$\bar{1}$0] and [$\bar{1}$2$\bar{1}$0] directions [Fig. 3(a)]. Both longitudinal (R_{long}) and transverse resistances (R_H) were measured with a rotating external field in the film plane, which aligns N perpendicular to the field orientation [Figs. 1(e) and 1(f)]. Consistent results have
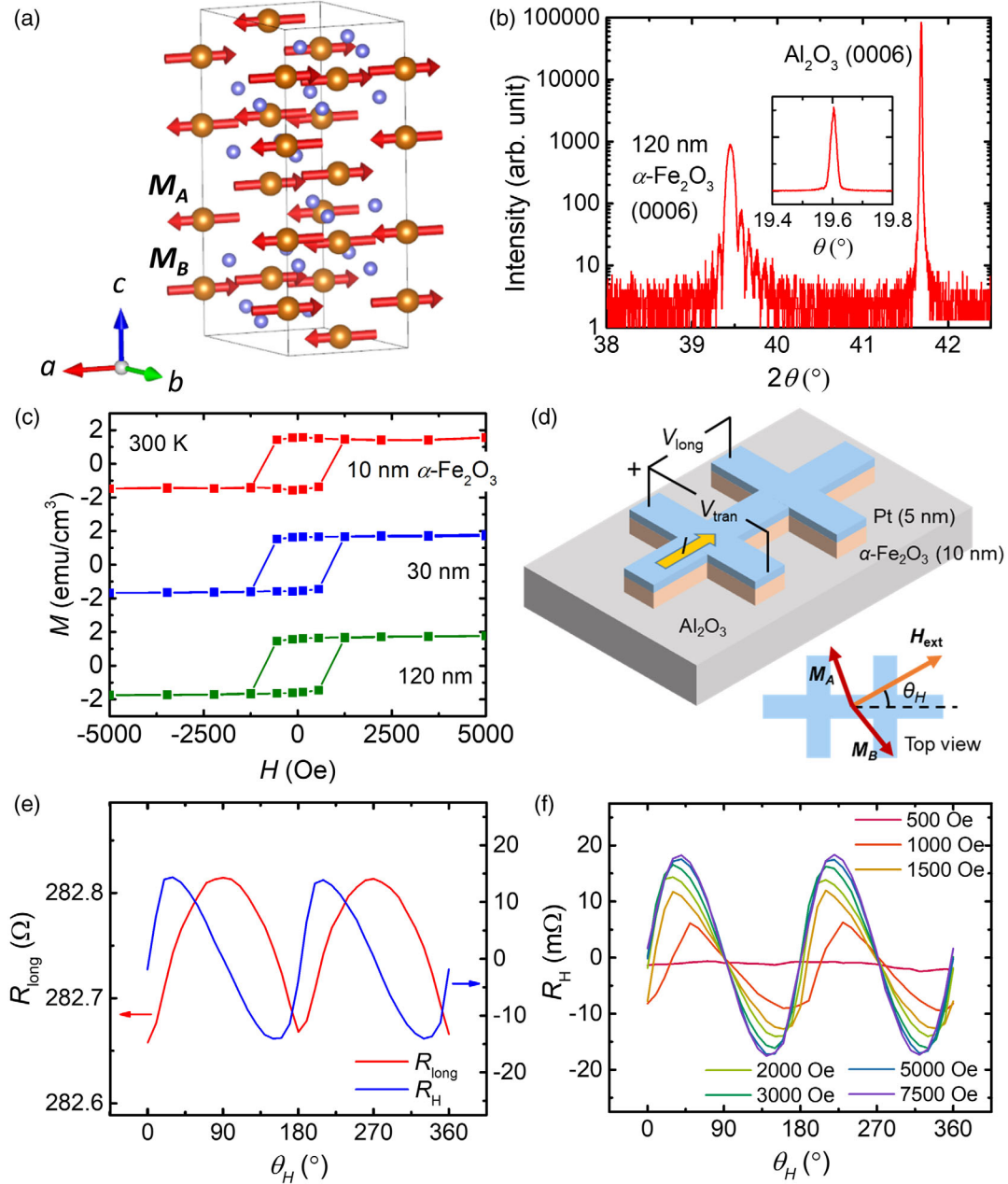
FIG. 1.   (a) Magnetic structure of α-Fe$_2$O$_3$. (b) X-ray diffraction of α-Fe$_2$O$_3$ (0001) film. (Inset) Rocking curve of the α-Fe$_2$O$_3$ (0006) peak. (c) SQUID magnetometry of α-Fe$_2$O$_3$ films for three different thicknesses. (d) Schematic of Hall bar device geometry and SMR measurement configuration. (Inset) Relative orientation between magnetic field and canted moments. (e) Longitudinal and transverse angle-dependent SMR under $H_{ext} = 2000$ Oe. The sensing current is along the $[\bar{1}2\bar{1}0]$ direction. (f) R_H under different in-plane fields.

been obtained for R_{long} and R_H measurements after taking into account geometrical factors. In the following, we will focus mostly on R_H measurement for monitoring magnetic dynamics. Close to saturation, R_H curves can be fitted by $R_H = (\Delta R_H/2)\sin(2\theta_H)$, where θ_H is the field angle defined in Fig. 1(d). Our SMR signal is consistent with previous findings in other antiferromagnetic insulators such as NiO and Cr$_2$O$_3$ [20–23]: R_{long} reaches maximum when N is collinear with the current. This is the opposite of the SMR

signal expected from a ferromagnet through the residual magnetic moment, suggesting the dominant role of the Néel vector in the SMR effect. The magnitude of SMR ($\Delta R_{long}/R_{long} \sim 0.06\%$) is also comparable to earlier reports in NiO [20,21].

We first tested the current-induced 90° Néel vector switching by following the procedures in Refs. [8] and [10]. As shown in Fig. 2(a), we send large current pulses with 10 ms pulse width that are oriented −45° (stage A) and
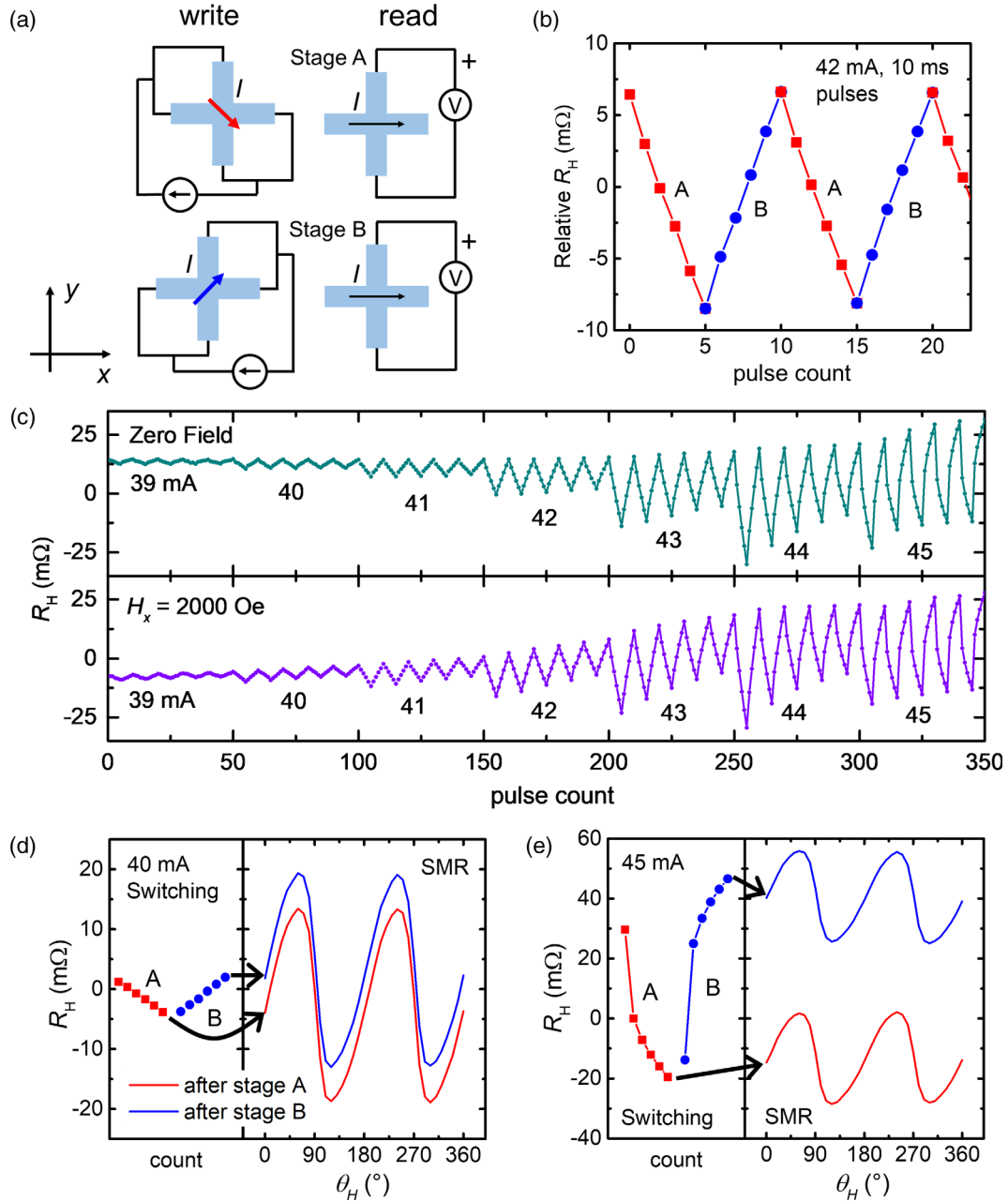
FIG. 2. (a) Schematics of the writing and reading procedures. (b) Example of R_H switching by current pulses. The red (blue) branches represent measured SMR signal in stage A (B). The lateral dimension of the Hall cross is $10 \times 60 \ \mu$m, and the α-Fe$_2$O$_3$ thickness is 10 nm. (c) Current-induced switching without and with $H_x = 2000$ Oe. (d),(e) Measurement of angle-dependent SMR signal after writing current pulses of 40 and 45 mA, respectively, showing that the resistance change is not related to the SMR change.

$+45°$ (stage B) from the horizontal direction to induce possible switching. According to the spin-orbit torque picture, this would flip N along the two orthogonal directions. To monitor the possible switching, we record R_H after each pulse with a small sensing current of 2 mA. To minimize thermally induced resistance variation, R_H is read after 10 s of waiting, allowing the device to return to equilibrium. As shown in Fig. 2(b), a periodic change in R_H is indeed observed. R_H repeatedly switches between low

and high values after applications of setting and resetting current pulses and forms a zigzag pattern.

The low spin-flop field in α-Fe$_2$O$_3$ allows us to control the Néel vector with a relatively small external field. Therefore, to check whether the observed switching has magnetic origins, we compared the current-induced R_H change with and without an external field. As shown in Fig. 2(c), across the whole current range, the switching behaviors under these two conditions are very similar.
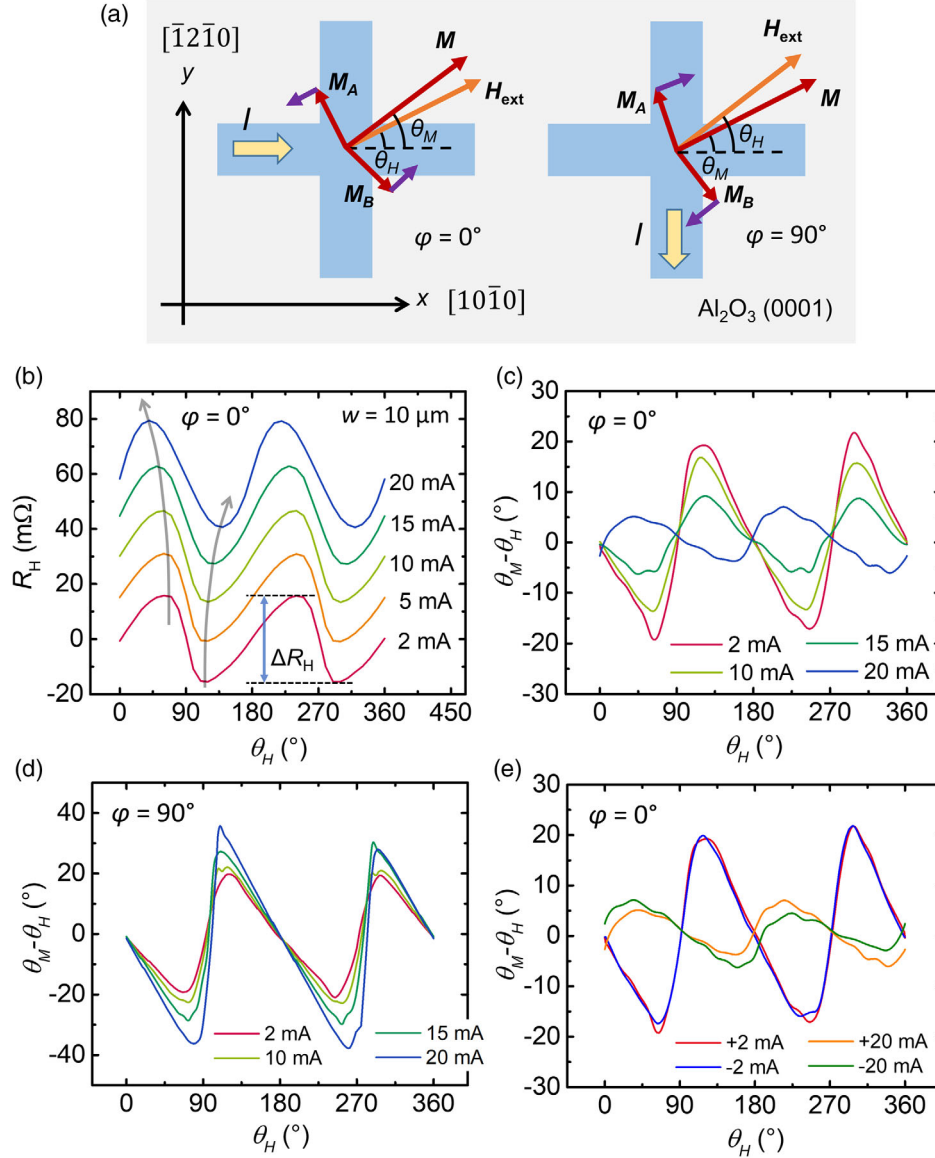
FIG. 3.   (a) Schematics of the magnetic moment tilting under applied currents. The left (right) panel is for current applied along the $x(y)$ axis [$\varphi = 0°$ (90°)]. The purple arrows on the sublattice moments indicate the tilting direction. Intrinsic magnetic anisotropy within the basal plane is neglected. (b) Angle-dependent SMR under different currents for $\varphi = 0°$. The gray arrows are guides for the eye, illustrating the shift of peak and valley. ΔR_H is defined in the figure. (c),(d) Angle between $\boldsymbol{M}$ and $\boldsymbol{H}$ as a function of θ_H for a range of applied currents at $\varphi = 0°$ and $\varphi = 90°$, respectively. The deviation of these curves from a perfectly smooth line shape reflects the magnetic domain pinning effect from defect. (e) Comparison of current-induced magnetic moment tilting under positive and negative currents for $\varphi = 0°$, as characterized by $\theta_M - \theta_H$. The results in Fig. 3 are obtained from a device with a lateral dimension of 10×60 μm and an α-Fe$_2$O$_3$ thickness of 10 nm.

The minor difference in the exact R_H value between the two curves is smaller than run-to-run variations under the same field condition. From this comparison, we see that the applied field, which is supposed to align the Néel vector and suppress the current-induced switching, turns out to have a negligible influence on the resistance change.

Furthermore, to understand the relationship between the resistance change and magnetic switching, we studied magnetic states after applied current pulses by measuring the angle-dependent SMR curves. In principle, if the switching behavior of Figs. 2(b) and 2(c) comes from the reorientation of the Néel vector, the resistance value after these pulses would correspond to a peak or valley position in the subsequent angle-dependent SMR curve. However, we found no obvious change in SMR signal, which always starts from zero and oscillates identically as the field rotates, regardless of the magnitude and direction of prior current pulses [Figs. 2(d) and 2(e)]. The main effect of the pulses is to cause an overall shift in the SMR curve. Under large writing pulses, this shift can become even

larger than the full range of field-induced SMR [Fig. 2(e)]. This independence between current-induced resistance switching and Néel vector reorientation suggests that, within our studied current range, the observed switching has a pure resistive origin. Sawtoothlike resistance switching has been previously utilized as an indication of magnetic reorientation in Pt/NiO systems [8,9]. Our results suggest that careful treatment is needed to distinguish whether the switching is of magnetic or nonmagnetic origin. One possible explanation for our observed sawtoothlike switching could be the electromigration effect from Pt wire [24]. We estimate that the current-induced temperature change can be as high as ∼150 K under the applied current [25], which is comparable to the values reported in previous memristive switching experiments with Pt [24].

The current-induced overall resistance shift represents an obstacle in revealing magnetic switching. To overcome this difficulty and search for possible features of the magnetic dynamics, we designed a new experiment which allows a demonstration of the magnetic switching tendency with smaller applied currents. Current-induced magnetic moment titling has been previously utilized in the second harmonic configuration for quantitative determination of spin torque in ferromagnets [13,14], as well as for a qualitative check on Néel vector switching in an antiferromagnet [3]. Here we measured the angle-dependent SMR curve subject to an in-plane rotating field by applying different sensing currents. If there is a current-induced field or torque effect which tends to switch the magnetic ordering, the Néel vector will be tilted away (or toward) the current direction [Fig. 3(a)]. This will be reflected as a deviation from the original angle dependence of the SMR signal, from which we can extract the nature and magnitude of the current's influence. Since we are focusing on the relative change of the SMR curve shape under constant currents, an overall shift due to resistive switching as in Fig. 2 does not make a contribution. Besides the current effect, we find that our α-Fe_2O_3 film always exhibits a constant, intrinsic easy-axis anisotropy within the basal plane due to the broken symmetry within the substrate, which favors $[\bar{1}2\bar{1}0]$ as an easy axis for the Néel vector [25]. This easy-axis anisotropy energy is determined to be ∼900 erg/cm^3 from our experiment. We note that our experimental approach below also applies to pristine α-Fe_2O_3 crystals with triaxial anisotropy within the basal plane [25].

The evolution of the SMR signal with various currents applied along the $+x$ direction on a sample with a 10 nm α-Fe_2O_3 and 10 μm channel width is shown in Fig. 3(b). The 2 mA curve is used as a baseline for its low current density (∼4×10^6 A/cm^2). As current increases, the field angle (θ_H) corresponding to the peak and valley locations shifts toward the x axis (the 0° and 180° direction), suggesting that a field that is closer to the x direction is needed to balance the current-induced effect for reaching the same SMR extrema. This observed trend, therefore,

implies that the current's effect tends to align M along the y axis (or equivalently N along the x axis since M and N are always perpendicular in this antiferromagnet). More quantitatively, the magnetic moment orientation θ_M can be determined from the SMR value together with the field scanning history information using the relationship of $R_H = (\Delta R_H/2)\sin(2\theta_M)$, where ΔR_H represents the peak to valley value under the lowest sensing current in Fig. 3(b). The current-induced Néel vector tilting can thus be characterized by the misalignment angle between M and H ($\theta_M - \theta_H$) as a function of θ_H [Fig. 3(c)]. We note that within the first half of the period ($\theta_H = 0°$–90°), $\theta_M - \theta_H$ becomes less negative as current increases and, at 20 mA, it even switches sign, suggesting that the current's effect is dominant over the intrinsic anisotropy under this current and that the x axis becomes more energetically favorable for N. To examine the relationship between the current's effect and its flowing direction, we vary the current direction φ. We first set $\varphi = 90°$ by applying I along $-y$. We find that the current's influence on magnetic anisotropy changes sign when compared with $\varphi = 0°$ case, and I now increases the intrinsic easy-axis anisotropy within the basal plane by tilting N further toward the y axis [Fig. 3(d)]. Next, we return to $\varphi = 0°$ but reverse the current direction; i.e., we apply I along $-x$ [Fig. 3(e)]. We find that the current-induced magnetic moment tilting shows similar trends under the reversal of current direction; i.e., both positive and negative currents induce an anisotropy along the x axis. However, under large currents, a small difference appears between $\pm I$. Within the field angle range of $\theta_H = 0°$–180°, the positive current-induced tilting of the Néel vector is larger, while it is smaller within $\theta_H = 180°$–360°. We also verify this current reversal effect by applying $\pm I$ under $\varphi = 90°$, where similar asymmetries were observed [25].

The current-induced magnetic moment titling shown in Figs. 3(b)–3(e) can be summarized as a change in a net magnetic energy in α-Fe_2O_3. Using its definition, we can extract this energy density [43] from the measured $\theta_M - \theta_H$ data through $E(\theta_M) = \mu_0 M H_{ext} \int_0^{\theta_M} \sin(\theta'_H - \theta'_M)d\theta'_M$, where μ_0 is the vacuum permeability, H_{ext} is the applied external field, and M is the net magnetization. $E(\theta_M)$ under a series of currents along the $+x$ ($-x$) direction are shown in Fig. 4(a) [Fig. 4(b)] for the same device. Based on the symmetry under current reversal, we can separate the current-induced energy change into two parts: the even component $\Delta E_{even} = [\Delta E(+I) + \Delta E(-I)]/2$ and the odd component $\Delta E_{odd} = [\Delta E(+I) - \Delta E(-I)]/2$. From Fig. 4, we see that ΔE_{even} follows $-\sin^2(\theta_M)$ under field rotation and has a 180° period, which represents a change in the uniaxial anisotropy, while ΔE_{odd} follows $\sin(\theta_M)$ and has a 360° period, which reflects a unidirectional magnetic energy (similar to a Zeeman energy). In the following, we will analyze the physics origin of these two effects.

First, to identify the origin of ΔE_{even}, we carried out a systematical study on ΔE_{even} as a function of device width
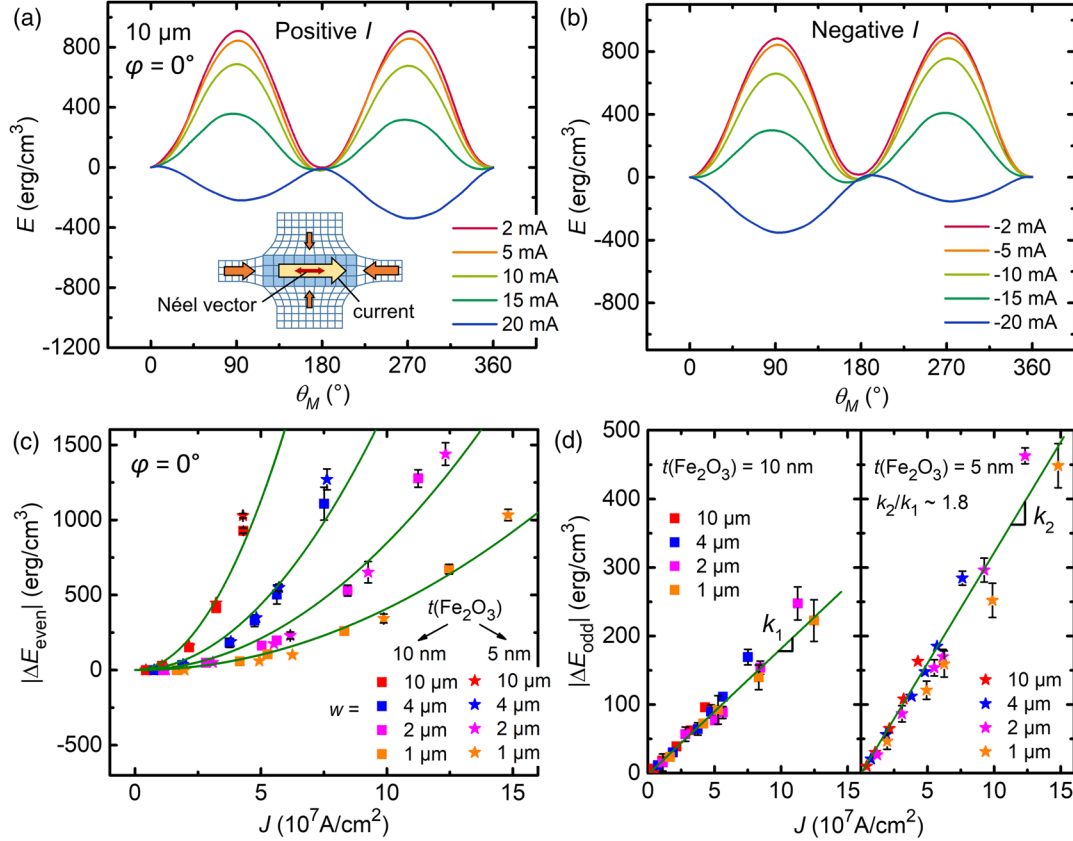
FIG. 4.   (a),(b) Angle-dependent magnetic energy as a function of applied currents for (a) positive and (b) negative current polarities, on a 10 μm sample for $\varphi = 0°$. [Inset of (a)] Schematic of the Joule-heating-induced magnetoelastic effect. (c),(d) The even and odd components of ΔE vs J for devices with different w and α-Fe$_2$O$_3$ thickness t(Fe$_2$O$_3$). The symbols and lines result from the experiment and the calculation, respectively. The slopes for $t = 10$ nm and $t = 5$ nm lines in (d) have the ratio 1.8.

w and α-Fe$_2$O$_3$ thickness t, as summarized in Fig. 4(c). ΔE_{even} shows a strong dependence on width w but is independent of thickness t. Both characteristics are inconsistent with the spin-orbit torque mechanism, as spin torque should depend only on J regardless of the channel width, and inversely proportional to the magnetic layer thickness. The results in Fig. 4(c), however, agree with a thermal mechanism picture. Particularly, the observed dependence on sample size is consistent with a Joule-heating-induced temperature increase, which has the form of $\Delta T \propto J^2 w$ [6,25,44]. While an overall temperature increase cannot explain the observed anisotropy energy change, Joule heating can lead to an additional contribution through magnetoelastic coupling. Under Joule heating, the substrate lattice constant under the device region will increase due to thermal expansion, resulting in a net compressive stress [Fig. 4(a) inset]. Moreover, similar to other antiferromagnetic insulators, α-Fe$_2$O$_3$ exhibits a fairly strong magnetoelastic effect with the reported [37,45] magnetostrictive coefficient λ_s on the order of 10^{-6}. Using a single parameter of $\lambda_s = 1.4 \times 10^{-6}$ as well as thermomechanical stress determined from finite element simulations [25], we find that the quadratic dependence of ΔE_{even} on J obtained from

devices with different w and t, and under different current directions and magnitudes [25], can all be well explained [see the solid curves in Fig. 4(c)].

We now turn to the odd component ΔE_{odd}. In contrast to ΔE_{even}, which shows a strong dependence on device size, ΔE_{odd} has the same linear dependence on J across devices with all different w [Fig. 4(d)], suggesting a nonthermal origin. As previously discussed, the $\sin(\theta_M)$ angle dependence of ΔE_{odd} in Figs. 4(a) and 4(b) is consistent with the characteristics of Zeeman energy. While either an Oersted field or a fieldlike torque τ_{FL} can contribute to this energy density, the comparison between the 5 and 10 nm thick α-Fe$_2$O$_3$ samples excludes the Oersted field as the main mechanism. By comparing the two slopes in Fig. 4(d), we find that, under the same current, ΔE_{odd} of the 5 nm sample is nearly twice the value of the 10 nm one, consistent with an interfacial mechanism like the spin-orbit torque. The small deviation from the expected factor of 2 might originate from an inaccuracy in thickness calibration. Moreover, from Fig. 4(d), we quantify the τ_{FL} efficiency in the 5 nm sample to be 25 Oe per 10^7 A/cm^2, which is about 7 times larger than the Oersted field. The magnitude of τ_{FL} here, when normalized with the magnetic film

thickness, is comparable to previously obtained values in ferromagnetic and ferrimagnetic insulators [13,26,46]. Finally, we note that, unlike τ_{FL}, which shows distinct symmetries from the current-induced magnetoelastic effect, the dampinglike torque τ_{DL} induces magnetic moment tilting with the same $\sin^2(\theta_M)$ angular dependence as the magnetoelastic effect [25]. As τ_{DL} is a function only of J and should not depend on w, we can estimate the upper bound of τ_{DL}'s contribution to the ΔE_{even} as ~ 150 erg/cm^3 at $J = 1 \times 10^8$ A/cm^2 from Fig. 4(c), which is lower than the magnetoelastic effect with our smallest w. As shown in our simulation, for easy-plane antiferromagnets with large magnetostrictive coefficients such as α-Fe$_2$O$_3$ and NiO [40,47] ($\lambda_s = 1$–5×10^{-4}), any influence from dampinglike torque can be dominated by the magnetoelastic effect in the current experimental configuration.

To summarize, we experimentally studied current-induced magnetic dynamics in a heavy metal–antiferromagnetic insulator bilayer system. By calibrating current-induced effects with a magnetic field, we identified the two main contributions of current and determined their magnitude: the magnetoelastic effect and fieldlike spin-orbit torque. The current-induced Néel vector tilting method enables the separation of real magnetic dynamics from nonmagnetic resistive switching. Meanwhile, a systematic study of the device size dependence of the current's effect allows us to tell the spin-orbit torque and thermal effect apart. These approaches are applicable to other easy-plane antiferromagnets, such as NiO, where the spin-flop field remains relatively small (on the order of 1 T) due to the weak anisotropy within the basal plane [25].

Note added.—Recently, we became aware of the related works of Refs. [48,49].

---

[*]luqiao@mit.edu

[1] P. Wadley *et al.*, Science **351**, 587 (2016).

[2] M. J. Grzybowski, P. Wadley, K. W. Edmonds, R. Beardsley, V. Hills, R. P. Campion, B. L. Gallagher, J. S. Chauhan, V. Novak, T. Jungwirth, F. Maccherozzi, and S. S. Dhesi, Phys. Rev. Lett. **118**, 057701 (2017).

[3] J. Godinho, H. Reichlová, D. Kriegner, V. Novák, K. Olejník, Z. Kašpar, Z. Šobáň, P. Wadley, R. P. Campion, R. M. Otxoa, P. E. Roy, J. Železný, T. Jungwirth, and J. Wunderlich, Nat. Commun. **9**, 4686 (2018).

[4] S. Y. Bodnar, L. Šmejkal, I. Turek, T. Jungwirth, O. Gomonay, J. Sinova, A. A. Sapozhnik, H. J. Elmers, M. Kläui, and M. Jourdan, Nat. Commun. **9**, 348 (2018).

[5] X. F. Zhou, J. Zhang, F. Li, X. Z. Chen, G. Y. Shi, Y. Z. Tan, Y. D. Gu, M. S. Saleem, H. Q. Wu, F. Pan, and C. Song, Phys. Rev. Applied **9**, 054028 (2018).

[6] M. Meinert, D. Graulich, and T. Matalla-Wagner, Phys. Rev. Applied **9**, 064040 (2018).

[7] S. Y. Bodnar, M. Filianina, S. P. Bommanaboyena, T. Forrest, F. Maccherozzi, A. A. Sapozhnik, Y. Skourski, M. Kläui, and M. Jourdan, Phys. Rev. B **99**, 140409(R) (2019).

[8] T. Moriyama, K. Oda, T. Ohkochi, M. Kimata, and T. Ono, Sci. Rep. **8**, 14167 (2018).

[9] X. Z. Chen, R. Zarzuela, J. Zhang, C. Song, X. F. Zhou, G. Y. Shi, F. Li, H. A. Zhou, W. J. Jiang, F. Pan, and Y. Tserkovnyak, Phys. Rev. Lett. **120**, 207204 (2018).

[10] L. Baldrati, O. Gomonay, A. Ross, M. Filianina, R. Lebrun, R. Ramos, C. Leveille, F. Fuhrmann, T. R. Forrest, F. Maccherozzi, S. Valencia, F. Kronast, E. Saitoh, J. Sinova, and M. Kläui, Phys. Rev. Lett. **123**, 177201 (2019).

[11] I. Gray, T. Moriyama, N. Sivadas, G. M. Stiehl, J. T. Heron, R. Need, B. J. Kirby, D. H. Low, K. C. Nowack, D. G. Schlom, D. C. Ralph, T. Ono, and G. D. Fuchs, Phys. Rev. X **9**, 041016 (2019).

[12] L. Liu, O. J. Lee, T. J. Gudmundsen, D. C. Ralph, and R. A. Buhrman, Phys. Rev. Lett. **109**, 096602 (2012).

[13] K. Garello, I. M. Miron, C. O. Avci, F. Freimuth, Y. Mokrousov, S. Blügel, S. Auffret, O. Boulle, G. Gaudin, and P. Gambardella, Nat. Nanotechnol. **8**, 587 (2013).

[14] M. Hayashi, J. Kim, M. Yamanouchi, and H. Ohno, Phys. Rev. B **89**, 144425 (2014).

[15] S. J. Williamson and S. Foner, Phys. Rev. **136**, A1102 (1964).

[16] P. R. Elliston and G. J. Troup, J. Phys. C **1**, 169 (1968).

[17] R. Lebrun, A. Ross, S. A. Bender, A. Qaiumzadeh, L. Baldrati, J. Cramer, A. Brataas, R. A. Duine, and M. Kläui, Nature (London) **561**, 222 (2018).

[18] P. J. Flanders and J. P. Remeika, Philos. Mag. **11**, 1271 (1965).

[19] N. Shimomura, S. P. Pati, Y. Sato, T. Nozaki, T. Shibata, K. Mibu, and M. Sahashi, J. Appl. Phys. **117**, 17C736 (2015).

[20] G. R. Hoogeboom, A. Aqeel, T. Kuschel, T. T. M. Palstra, and B. J. Van Wees, Appl. Phys. Lett. **111**, 052409 (2017).

[21] J. Fischer, O. Gomonay, R. Schlitz, K. Ganzhorn, N. Vlietstra, M. Althammer, H. Huebl, M. Opel, R. Gross, S. T. B. Goennenwein, and S. Geprägs, Phys. Rev. B **97**, 014417 (2018).

[22] L. Baldrati, A. Ross, T. Niizeki, C. Schneider, R. Ramos, J. Cramer, O. Gomonay, M. Filianina, T. Savchenko, D. Heinze, A. Kleibert, E. Saitoh, J. Sinova, and M. Kläui, Phys. Rev. B **98**, 024422 (2018).

[23] Y. Ji, J. Miao, Y. M. Zhu, K. K. Meng, X. G. Xu, J. K. Chen, Y. Wu, and Y. Jiang, Appl. Phys. Lett. **112**, 232404 (2018).

[24] T. Kozlova, M. Rudneva, and H. W. Zandbergen, Nanotechnology **24**, 505708 (2013).

[25] See Supplemental Material at http://link.aps.org/supplemental/10.1103/PhysRevLett.123.247206, which includes Refs. [26–42], for details on material characterization, SMR data process, macrospin simulation, thermal stress analysis, and other related studies.

[26] J. Li, G. Yu, C. Tang, Y. Liu, Z. Shi, Y. Liu, A. Navabi, M. Aldosary, Q. Shao, K. L. Wang, R. Lake, and J. Shi, Phys. Rev. B **95**, 241305(R) (2017).

[27] M. H. Nguyen, D. C. Ralph, and R. A. Buhrman, Phys. Rev. Lett. **116**, 126601 (2016).

[28] E. Sagasta, Y. Omori, M. Isasa, M. Gradhand, L. E. Hueso, Y. Niimi, Y. Otani, and F. Casanova, Phys. Rev. B **94**, 060412(R) (2016).

[29] C. O. Avci, A. Quindeau, C. F. Pai, M. Mann, L. Caretta, A. S. Tang, M. C. Onbasli, C. A. Ross, and G. S. D. Beach, Nat. Mater. **16**, 309 (2017).

[30] C. F. Pai, Y. Ou, L. H. Vilela-Leão, D. C. Ralph, and R. A. Buhrman, Phys. Rev. B **92**, 064426 (2015).

[31] D. Lu, D. I. Florescu, D. S. Lee, V. Merai, A. Parekh, J. C. Ramer, S. P. Guo, and E. Armour, Phys. Status Solidi A **200**, 71 (2003).

[32] A. H. Hill, F. Jiao, P. G. Bruce, A. Harrison, W. Kockelmann, and C. Ritter, Chem. Mater. **20**, 4891 (2008).

[33] K. Mizushima and S. Iida, J. Phys. Soc. Jpn. **21**, 1521 (1966).

[34] P. J. Besser, A. H. Morrish, and C. W. Searle, Phys. Rev. **153**, 632 (1967).

[35] O. Gomonay, V. Baltz, A. Brataas, and Y. Tserkovnyak, Nat. Phys. **14**, 213 (2018).

[36] O. R. Sulymenko, O. V. Prokopenko, V. S. Tiberkevich, A. N. Slavin, B. A. Ivanov, and R. S. Khymyn, Phys. Rev. Applied **8**, 064007 (2017).

[37] H. Porath, Philos. Mag. **17**, 603 (1968).

[38] E. Ressouche, N. Kernavanois, L. P. Regnault, and J. Y. Henry, Physica (Amsterdam) **385B-386B**, 394 (2006).

[39] R. Gaillac, P. Pullumbi, and F. X. Coudert, Phys. Condens. Matter **28**, 275201 (2016).

[40] N. B. Weber, H. Ohldag, H. Gomonaj, and F. U. Hillebrecht, Phys. Rev. Lett. **91**, 237205 (2003).

[41] F. L. A. Machado, P. R. T. Ribeiro, J. Holanda, R. L. Rodríguez-Suárez, A. Azevedo, and S. M. Rezende, Phys. Rev. B **95**, 104418 (2017).

[42] E. Uchida, N. Fukuoka, H. Kondoh, T. Takeda, Y. Nakazumi, and T. Nagamiya, J. Phys. Soc. Jpn. **23**, 1197 (1967).

[43] J. Stöhr and H. C. Siegmann, *Magnetism: From Fundamentals to Nanoscale Dynamics* (Springer Berlin, 2006).

[44] C. You, I. M. Sung, and B. Joe, Appl. Phys. Lett. **89**, 222513 (2006).

[45] R. A. Voskanyan, R. Z. Levintin, and V. A. Shchurov, Sov. Phys. JETP **27**, 423 (1968).

[46] J. Finley, C. H. Lee, P. Y. Huang, and L. Liu, Adv. Mater. **31**, 1805361 (2019).

[47] K. Nakahigashi, N. Fukuoka, and Y. Shimomura, J. Phys. Soc. Jpn. **38**, 1634 (1975).

[48] Y. Cheng, S. Yu, M. Zhu, J. Hwang, and F. Yang, arXiv:1906.04694.

[49] C. C. Chiang, S. Y. Huang, D. Qu, P. H. Wu, and C. L. Chien, Phys. Rev. Lett. **123**, 227203 (2019).